Modeling the Ries–Steinheim impact event and the formation of the moldavite strewn field

DIETER STÖFFLER[1]*, NATALIA A. ARTEMIEVA[2] AND ELISABETTA PIERAZZO[3]

[1]Institut für Mineralogie, Museum für Naturkunde, Humboldt-Universität zu Berlin, Invalidenstrasse 43, D-10099 Berlin, Germany
[2]Institute for Dynamics of Geospheres, Russian Academy of Sciences, Leninsky Prospect 38/6, Moscow, Russia 117939
[3]Planetary Science Institute, 620 North 6th Street, Tucson, Arizona 85705, USA
*Correspondence author's e-mail address: dieter.stoeffler@rz.hu-berlin.de

Abstract–Using detailed geological, petrographic, geochemical, and geographical constraints we have performed numerical modeling studies that relate the Steinheim crater (apparent diameter D_a = 3.8 km), the Ries crater (D_a = 24 km) in southern Germany, and the moldavite (tektite) strewn field in Bohemia and Moravia (Czech Republic), Lusatia (East Germany), and Lower Austria. The moldavite strewn field extends from ~200 to 450 km from the center of the Ries to the east-northeast forming a fan with an angle of ~57°. An oblique impact of a binary asteroid from a west-southwest direction appears to explain the locations of the craters and the formation and distribution of the moldavites. The impactor must have been a binary asteroid with two widely separated components (some 1.5 and 0.15 km in diameter, respectively). We carried out a series of three-dimensional hydrocode simulations of a Ries-type impact. The results confirm previous results suggesting that impacts around 30–50° (from the horizontal) are the most favorable angles for near-surface melting, and, consequently for the formation of tektites. Finally, modeling of the motion of impact-produced tektite particles through the atmosphere produces, in the downrange direction, a narrow-angle distribution of the moldavites tektites in a fan like field with an angle of ~75°. An additional result of modeling the motion of melt inside and outside the crater is the preferred flow of melt from the main melt zone of the crystalline basement downrange towards the east-northeast rim. This explains perfectly the occurrence of coherent impact melt bodies (some tens of meters in size) in a restricted zone of the downrange rim of the Ries crater. The origin of these melt bodies, which represent chemically a mixture of crystalline basement rocks similar to the main melt mass contained (as melt particles <0.5 m in size) in the suevite, do not occur at any other portion of the Ries crater rim and remained enigmatic until now. Although the calculated distribution of moldavites still deviates to some degree from the known distribution, our results represent an important step toward a better understanding of the origin and distribution of the high-velocity surface melts and the low-velocity, deep-seated melt resulting from an oblique impact on a stratified target.

INTRODUCTION

Since 1963 when the first radiometric ages became available (Gentner *et al.*, 1963), there has been a general agreement that the impact craters Ries and Steinheim (24 and 3.8 km in diameter, respectively), southern Germany, and the moldavite strewn field (Bohemia, Moravia, Lusatia, and Lower Austria, east to northeast of Ries and Steinheim; Fig. 1) were formed in a single impact event some 15.0 Ma ago (Gentner *et al.*, 1963; Bolten and Müller, 1969; Gentner and Wagner, 1969; Pohl *et al.*, 1977; Reiff, 1979 and references therein; Staudacher *et al.*, 1982; Stöffler and Ostertag, 1983; Lange, 1996). Regarding the ejection mechanics of moldavites only a few older studies

are available (Vand, 1963; David, 1966). Despite some 40 years of modern research there is no comprehensive understanding of how the double crater and the tektites formed in a single collision event although for the Ries crater an oblique impact from the north has been proposed by Graup (1999) on the basis of the distribution of different types of suevites (with and without immiscible carbonate melts).

We have started a numerical modeling project for the Ries–Steinheim–moldavite event (Pierazzo *et al.*, 2001; Stöffler *et al.*, 2001, 2002) utilizing a very detailed geological, petrographic, and geochemical database that is available for this very unique impact event. We believe that such a case study will contribute to some fundamental aspects of impact
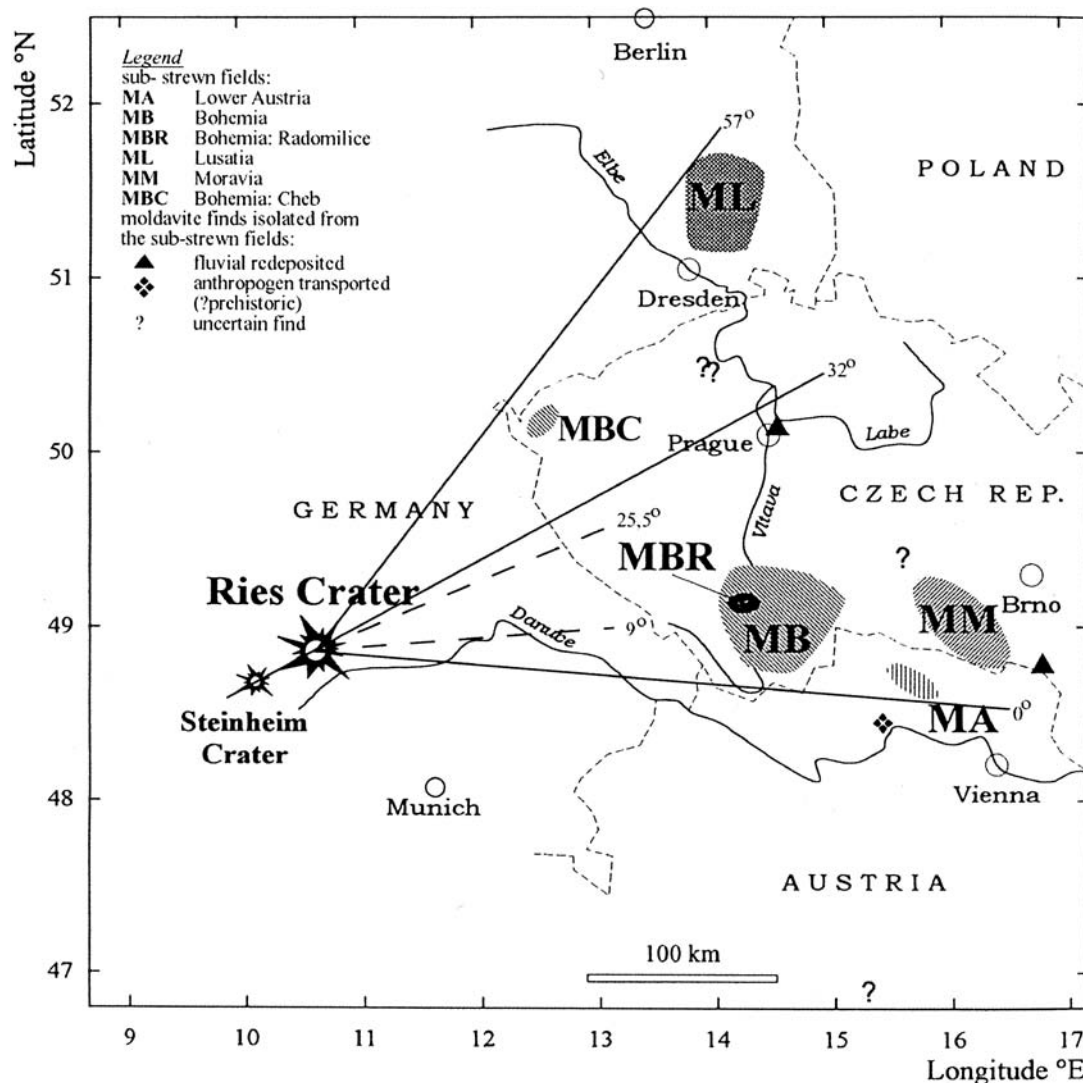
FIG. 1. Map of Central Europe showing the Ries and Steinheim craters and the moldavite strewn field (modified after Lange, 1996); the sub-strewnfields are hatched and explained in the legend; dashed lines (9 to 25.5°) define the fan within which coherent melt patches are observed on the inner slope of the Ries crater rim.

cratering, such as (1) impact on a complex stratified target, including the direction, angle, and velocity of impact, of relative size and nature of impactors, and the role of the atmosphere and of the target composition, (2) production and distribution of early and late melt ejecta from oblique impacts: formation, ejection, and distribution of "shallow" tektite melt and of the "deep-seated" major impact melt mass.

GEOGRAPHIC AND AGE CHARACTERISTICS OF THE CRATERS AND OF THE DIFFERENT TYPES OF EJECTED IMPACT MELT

Biostratigraphic ages of the oldest post-impact lake sediments at the Ries and Steinheim are indistinguishable from each other (Bolten and Müller, 1969; Groschopf and Reiff,

1971). The Ries glass bombs in the suevite and the moldavites have an ^{40}Ar-^{39}Ar and a fission track age of 15.0 Ma (Gentner et al., 1963; Gentner and Wagner, 1969; Staudacher et al., 1982; Vennemann et al., 2001). Unfortunately, there is no melt to be dated radiometrically at the Steinheim basin. These age data provide strong evidence for a cogenetic origin of all three impact features (Stöffler and Ostertag, 1983; Horn et al. 1985). Geographically, these features are arranged along a west-southwest–east-northeast line with Steinheim at the western end and the Ries center some 42 km east-northeast of Steinheim; the moldavites occur some 200 to 450 km east to northeast from the Ries center (Table 1) forming a fan of ~57° (centered at the Ries; see Figs. 1 and 2). This fan is symmetrically arranged along the east-northeast Steinheim–Ries connection line with the highest concentration of moldavites in the eastern
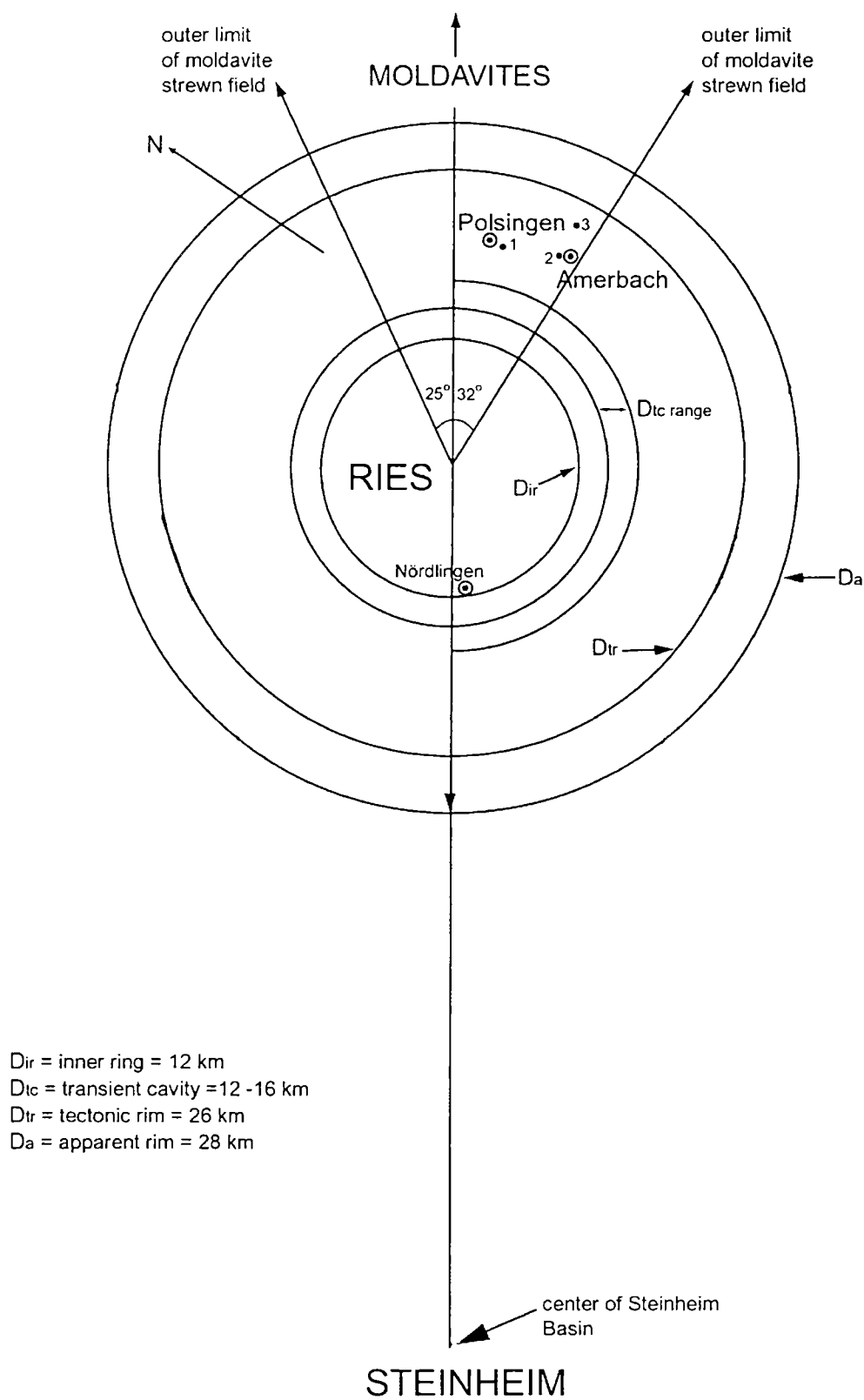
FIG. 2. Geographic relations between Steinheim, Ries, coherent melt ejecta at the east-northeast rim of Ries, and ejecta fan of the moldavites; 1, 2 and 3 are the localities of coherent melt patches (1 = Polsingen quarry, 2 = Amerbach road cuts (not exposed anymore), and 3 = Rauhwinkel); note arrow for north.

TABLE 1. Distance ranges of moldavite tektites from the Ries center after Lange (1996) and Lange (1990).

Moldavite region	Distance range (km)*	Distance range (km)†
Cheb/Eger	195	–
Bohemia	260–330	255–305
Moravia	390–455	385–415
Lower Austria	360–390	350–370
Lusatia (East Germany)	350–400	340–390

*Lange (1996).
†Lange (1990).

part of the fan, and distinctively less moldavite mass in the northeast part. This fact became clear only more recently when moldavites were discovered in East Germany (Lange, 1990) and in Lower Austria (Koeberl *et al.*, 1988). In addition, the only known occurrences of coherent impact melt breccias (melt rocks with crystalline matrix) in the Ries, observed as large patches of several tens of meters in size, are located within the southern part of this fan, on the inner slope of the eastern Ries crater rim (Engelhardt *et al.*, 1969;

Fig. 2). The very asymmetric distribution of these few melt bodies is in distinct contrast to the distribution of the main mass of crystalline basement melt, which is contained as particles in the suevite, whose distribution around the whole crater is more or less symmetrical (Hüttner and Schmidt-Kaler, 1999).

THE PRE-IMPACT STRATIGRAPHY

The target rocks of both the Ries and Steinheim craters at the time of impact consisted respectively of a ~620 and ~1180 m thick, horizontally layered sequence of Tertiary, Jurassic and Triassic sedimentary rocks (limestone, shale, sandstone) and possibly some minor Permian sediments. This sedimentary rock sequence is underlain by crystalline rocks (gneisses, granites, metabasites) of Hercynian age (*e.g.*, Graup, 1978; Hüttner and Schmidt-Kaler, 1999). The basement is involved in the cratering event only in the Ries. Tertiary sand, clay, and freshwater limestone formed a discontinuous layer at the pre-impact surface of the Ries (0–50 m thick; *e.g.*, Hüttner and Schmidt-Kaler, 1999) on top of Upper Malmian limestone. Figure 3a and Table 2 shows the stratigraphy at the Ries, which has been used to construct a "simplified" model stratigraphy for the hydrocode simulations (Fig. 3b).

TABLE 2. Stratigraphy and lithologies of the Ries pre-impact target (modified from Hüttner and Schmidt-Kaler, 1999).

Stratigraphic sections and thickness (m)*	Subdivisions and lithologies	Thickness (m)*
Tertiary 0–50	Middle Miocene = sands with minor clay and freshwater limestone	0–50
Malmian 150–200	ϵ = massive limestone	~20
	δ = massive limestone	70–100
	γ = bedded limestone with some marly limestone, marl and some reef limestone	~30
	β = mainly bedded limestone	~20
	α = marly limestone, marl, bedded limestone	40–50
Dogger 140–150	γ–ζ = limestone, calcareous limestone and shale	~10
	β = sandstone, in part iron-rich	~40
	α = gray shale	90–100
Liassic 30	Black shale with some sandstone and marl	~30
Triassic 250–300	Upper Keuper = red shale	~30
	Middle Keuper = sandstone with some shale	~200
	Muschelkalk = calcareous sandstone	0–50
	Buntsandstein ?	up to 15?
Hercynian basement	Various gneisses, granites, amphibolites	several kilometers

*Range of estimates for the pre-impact target at the point of impact.

a) Pre-impact stratigraphy
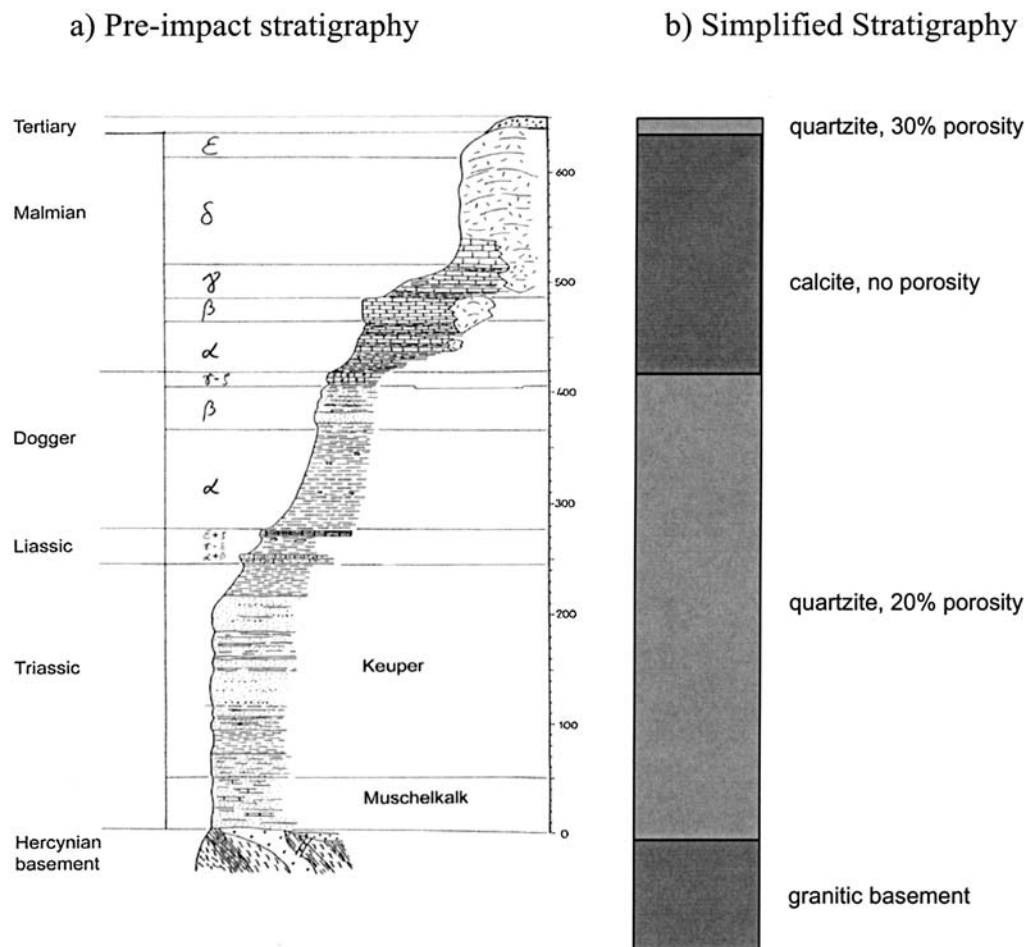
b) Simplified Stratigraphy

FIG. 3. (a) Reconstructed pre-impact stratigraphy of the Ries region (from Hüttner and Schmidt-Kaler, 1999); details of the lithologies are given in Table 2; (b) model stratigraphy implemented in the hydrocode simulations (see also Table 3).

DISTRIBUTION OF CLASTIC EJECTA AND IMPACT MELTS

The displaced rocks of the Steinheim and Ries craters are dominated by rocks from the sedimentary sequence. The deepest rocks excavated at Steinheim are Dogger sandstone (from about 380–430 m depth) and crystalline rocks at the Ries (from about 1500–2000 m depth) (Stöffler and Ostertag, 1983). The ejecta blanket of the Steinheim basin is completely eroded and no impact melt is found; obviously the melt zone was confined mainly to carbonates. Large parts of the Ries' continuous ejecta blanket are preserved consisting of a polymict lithic, clastic matrix breccia (bunte breccia, <200 m thick) covered by "fallout" suevite patches ranging in thickness from ~5 to 90 m (Stöffler and Ostertag, 1983; Engelhardt, 1997). Bunte breccia and suevite extend radially to ~45 and 23 km, respectively (Hüttner and Schmidt-Kaler, 1999).

Distal, discontinuous ejecta are composed of Upper Jurassic limestone clasts ("Reuter blocks", centimeter to decimeter sized; Gall and Müller, 1975) at a radial range of ~50 to 70 km, and

moldavite tektites some 200 to 450 km (Table 1) from the point of impact (Stöffler and Ostertag, 1983; Lange, 1996), as shown in Fig. 1. As indicated by its chemical and isotopic composition the moldavite melt originates from the top 50 m of mainly sandy Tertiary deposits of the Ries target, with minor additions of clay and freshwater limestone (Engelhardt, 1972; Engelhardt et al., 1987; Horn et al., 1985). The second type of impact melt, confined to the interior crater and the suevite of the ejecta blanket, is derived from crystalline basement from the main melt zone of the Ries crater (Graup, 1978). The chemical composition of the basement melt is rather homogeneous and reflects a mixture of different rocks, mainly granite and biotite-plagioclase gneiss (Engelhardt, 1967, 1972; Stähle, 1972; Vennemann et al., 2001). Most of this melt is contained in the suevite (central basin and "fallout" suevite) as melt particles <50 cm in size. A layer of coherent melt rocks is missing in the Ries crater (Pohl et al., 1977; Kieffer and Simonds, 1980); however, several patches of coherent melt ("red", clast-rich, crystallized melt breccia, ~50 m in size) are known to occur at the inner slope of the eastern crater rim near Polsingen,

Amerbach, and Rauhwinkel (Schnell, 1926; Engelhardt *et al.*, 1969; B. O. Dressler, pers. comm.). They are chemically identical to the melt contained in the suevite and are located inside the east to east-northeast part of the fan of melt ejecta defined by the periphery of moldavite strewn field (Fig. 2). This type of melt is not found anywhere else in the Ries.

THE RIES–STEINHEIM IMPACTOR

We integrated the equation of motion of a body (an asteroid is assumed based on the data of Morgan *et al.*, 1979) in the atmosphere (*e.g.*, see Passey and Melosh, 1980) to determine whether major fragments of an asteroid that broke up in the atmosphere could separate sufficiently to create the Ries–Steinheim double crater. The equation of motion includes atmospheric drag, planetary gravitational acceleration, and a fictious centrifugal force added to compensate for the curvature of the spherical Earth (*e.g.*, Passey and Melosh, 1980). We assumed that breakup occurred at an altitude between 50 and 100 km, but the results do not change significantly by increasing the altitude. In this approach we do not include separation mechanisms like shock wave interaction, asteroid rotation, or lift forces (*e.g.*, Artemieva and Shuvalov, 2001). These mechanisms become important only for rather small, meter-sized fragments (Artemieva and Shuvalov, 2001) and can be neglected in the present study because the smaller object is of the order of 100 m in diameter. The trajectories of the two bodies, whose sizes are similar to the Ries and Steinheim impactors (~1000 and 100 m, respectively), were followed for different impact angles and impact velocities, to determine how far they could separate upon reaching the Earth's surface. We used a typical density of 2.5 g/cm³ for the two bodies, although we also explored how a lower density (2 g/cm³) for the larger (Ries-size) body would affect the results. The entry velocity was varied between 11.2 km/s (Earth's escape) and 22 km/s, and the entry angle (measured from the surface) from 60° to 10°. Since both the Ries and Steinheim do appear circular, the possibility of a highly oblique impact (<10°) must be excluded. The results indicate that the separation between the two objects increases with decreasing impact angle and impact velocity. However, the maximum separation at the surface is some hundreds of meters, more than 2 orders of magnitude smaller than the distance between the Ries and the Steinheim craters (~42 km). Changing density for the larger body does not affect the overall outcome. Therefore, the Ries–Steinheim craters could not have been formed as a result of the breakup of an asteroid upon entering the Earth's atmosphere or by a contact binary asteroid (see also Melosh and Stansberry, 1991). The alternative is that they were formed by a binary object with a pre-atmospheric entry separation at least similar to the distance between the two craters, consistent with the results of Melosh and Stansberry (1991). This makes for a rather unusual binary object, in which one object is an order of magnitude smaller than the other (binaries observed so far tend

to have a secondary/primary size ratio of about one-third, and typical separations are few primary radii; Margot *et al.*, 2002).

Because of the large physical separation of the two craters, most probably any interaction between the two simultaneous impact events took place only at a late stage, as shock waves decay rather quickly into seismic waves. In general, shock pressure drops below 0.1 GPa at a distance which is 50–100× the projectile radius (Melosh, 1989; Ahrens and O'Keefe, 1977). It is also improbable that any interaction occurred between the expansion plumes generated by the impacts, as the Steinheim basin is small enough that its expansion plume would decelerate within one atmospheric scale height (~8 km). However, the ballistic ejecta of both craters could have interfered with each other. Such effects are probably erased by later erosion although distal Ries ejecta could be searched for in drill cores of the inner breccia lens of the Steinheim basin.

HYDROCODE MODELING

All results presented below relate to the Ries crater and its impact melts, specifically to the initial stage of the Ries crater growth, when the pressures are rather high and allow for simplified hydrodynamic (without material strength) description. This treatment is sufficient for simulating melt production and melt ejection. A complete numerical description of the Ries crater formation (*i.e.*, including crater collapse) would require a detailed treatment of strength and of the rheological properties of the complex Ries target (currently there is no hydrocode that can model accurately both the early and late stage of crater formation).

Our impact simulations were carried out with the three-dimensional hydrocode SOVA (Shuvalov, 1999) coupled to ANEOS-derived (Thompson and Lauson, 1972) equation of state tables for the materials used in the simulations. SOVA is a two-step Eulerian code that can model multidimensional, multimaterial, large deformation, strong shock wave physics. It is based on the same principles utilized in the well-known code CTH (McGlaun *et al.*, 1990). Three-dimensional comparison simulations between SOVA and CTH (Pierazzo *et al.*, 2001) show that results from SOVA are similar to those from CTH, but are characterized by better efficiency (faster runs for same spatial resolution), making SOVA a better choice for extensive parametric simulations like those necessary for this study. To model the various materials of interest we used tables derived from the ANEOS equation of state package (Thompson and Lauson, 1972). The use of tables, rather than the full ANEOS equation of state, allows us to further speed up the computation time, which is crucial for extended high-resolution three-dimensional simulations. A feature that makes SOVA unique among hydrocodes used for impact cratering studies is the implementation of a procedure to describe particle motion in the evolving ejecta-gas plume, including the interaction of particles with the gas.

The target layout, shown in Fig. 3b, has been reconstructed and simplified from the known pre-impact stratigraphy shown in Fig. 3a (Hüttner and Schmidt-Kaler, 1999; Stöffler et al., 2001). It consists of a 600 m thick sedimentary layer divided into, from top to bottom: 40 m of quartzite with 30% porosity (density of 1.86 g/cm³) to model the uppermost Tertiary sands (ANEOS equation of state from Melosh, pers. comm.); 140 m of non-porous calcite (density of 2.6 g/cm³; Pierazzo et al., 1998) to model the Malmian limestone; 420 m of quartzite with 20% porosity (density of 2.12 g/cm³) to model the Jurassic/Triassic sands and shales. The crystalline basement below the sedimentary layer is modeled as non-porous granite (Pierazzo et al., 1997). Table 3 summarizes the target layout used in the hydrocode simulations. It should be mentioned that the thickness of the uppermost sands is poorly known and, most probably, it was not constant over the whole impact area. Thus, our choice of 40 m layer may be considered as an upper limit for this layer. Since only three different materials are currently allowed in SOVA (which allows a rigorous mathematical treatment of mixed cells in the simulations), we model the atmosphere as pure CO_2 (i.e., decomposed calcite), instead of real air, and the projectile as granite (the same EOS as for crystalline basement) with 5% porosity (corresponding to a bulk density of 2.5 g/cm³).

The simulations model spherical asteroids striking the Earth's surface at angles of 45°, 30°, and 15° from the surface with velocities of 12, 20 and 40 km/s. To insure that all the simulations model a similar transient cavity diameter (between 12 and 13 km; Hörz et al., 1983), the projectile sizes have been varied according to the Pi-scaling law (Schmidt and Housen, 1987), and are shown in Table 4. Spatial resolution has been

optimized to best reflect the target lithology, and varied from 10 m, to resolve the thin surface layers, to 60 m at a depth of ~1 km. A few rezoning procedures which increase cell size have been made at later stages. The use of bilateral symmetry allowed us to model the $y > 0$ semispace only, and thus to take advantage of the available computer capacity for a higher resolution near the impact site. Since the simulations start with the projectile close to the surface, we do not consider the atmospheric wake (i.e., the "hole" punched in the atmosphere by the entering projectile) and its interaction with the ejecta. However, this is not an important mechanism for oblique impacts (as it is for vertical impacts, where the post-impact flow develops entirely inside the wake (e.g., Artemieva and Shuvalov, 1994)), as the post-impact flow develops in the downrange direction, opposite to the location of the wake.

MELT PRODUCTION

Figure 4 shows the early stages of impact ($t \approx 0.5$ s) for a 20 km/s impact at 15°, 30°, and 45° from the surface (projectile was coming from the left). All the colors are graded according to density variations. Impact angle affects the melting and early ejection of material from the crater. Figure 4 also suggests that impact angle strongly affects the shape of the opening cavities; however, this is true only for the very early stages of the impact event. The final crater shape depends on the late stage of excavation and collapse, for which the impact direction is not an important parameter (at least for impact angles above ~15°).

For each simulation, we estimated the amount of melting of the various layers modeled, including the crystalline basement. This has been done by marking each computational cell with a

TABLE 3. Target layout for the Ries hydrocode modeling (see Fig. 3b).

Material	Depth (km)	Density (g/cm³)	Porosity (%)	ANEOS	Reference
Tertiary sands	0.00–0.04	1.86	30	quartzite	Melosh, pers. comm.
Malmian limestone	0.04–0.18	2.6	0	calcite	Pierazzo et al. (1998)
Jurassic/Triassic sandstone	0.18–0.60	2.12	20	quartzite	Melosh, pers. comm.
Crystalline basement	0.60–20.0	2.63	0	granite	Pierazzo et al. (1997)

TABLE 4. Amount of melt + vapor (in km³) produced in the hydrocode simulations for the various target layers.

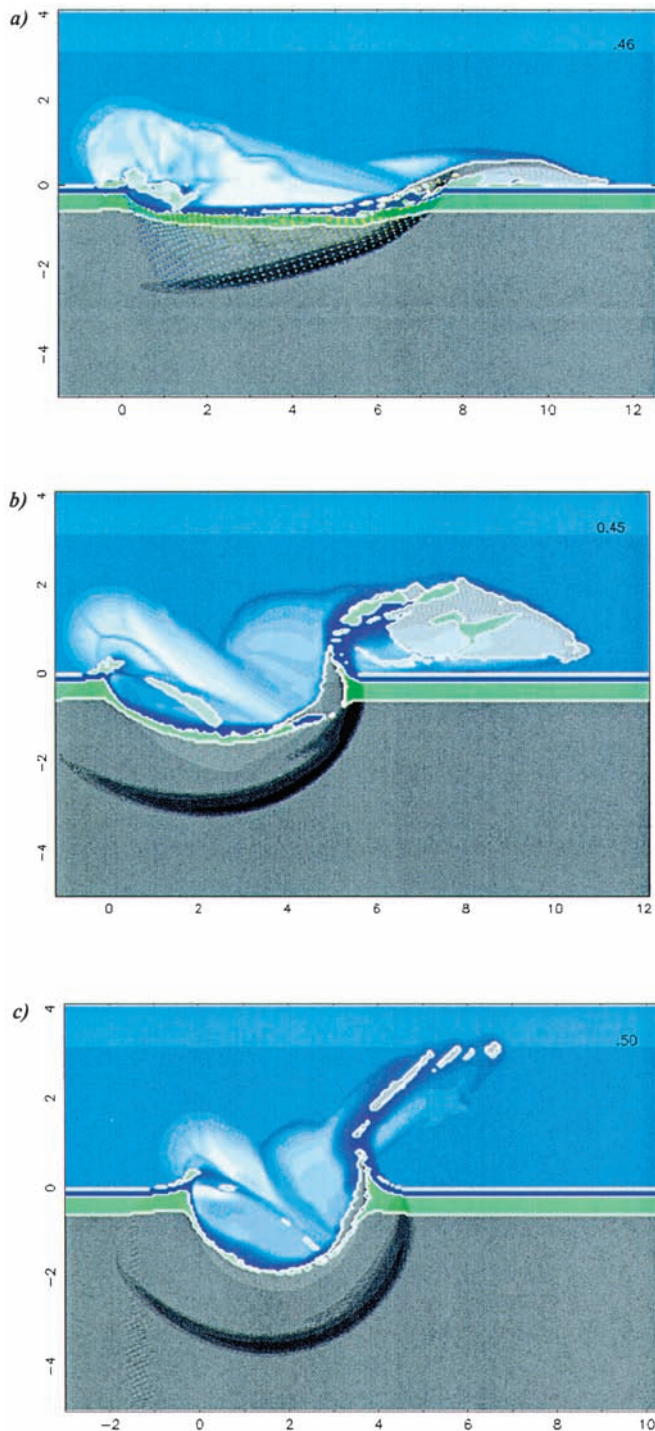| Impact velocity	12 km/s		20 km/s			40 km/s
Angle	30°	45°	15°	30°	45°	45°
D_{pr} (km)	1.9	1.6	2.1	1.5	1.2	0.8
Sands (40 m)	0.39	0.21	0.67	0.37	0.23	0.21
Limestone (140 m)	0.98	0.57	2.15	1.14	0.58	0.49
Sandstone (420 m)	5.39	3.73	7.92	6.27	3.77	3.38
Basement	6.70	7.20	9.20	13.44	9.72	8.22
Total	13.46	11.71	19.94	21.22	14.30	12.30

FIG. 4. Initial stages (~0.5 s) of impact simulations for various impact angles: (a) 15°, (b) 30°, and (c) 45°, for a 20 km/s impact (Table 4). The crystalline basement is shown in gray, quartzite in green, and calcite in dark blue. The atmosphere is shown in blue. All colors are graded according to density variations.

Lagrangian massless tracer particle that records the thermodynamic history of the material in the cell. Figure 5 shows the distribution of shock pressure in the target region for a 45°, 20 km/s impact; the left side shows the shock compression with respect to the pre-impact target (useful to estimate the volume of target subject to a given shock pressure); on the right is the real distribution of shocked material as the crater opens up, ~5 s after the impact. The amount of melting and vaporization is determined by adding up the initial volume of cells whose tracers record shock pressures above a given threshold. We used 55 GPa as the threshold for shock degassing of non-porous calcite (140 m limestone layer). For 30% (upper 40 m sands) and 20% (420 m Jurassic/Triassic layer) porous quartzite the ANEOS-based shock pressure for complete melting is 20 and 32 GPa, respectively, while it is 40 and 52 GPa for incipient vaporization. Finally, the ANEOS-based shock pressure for complete melting of granite (dense crystalline basement) is 56 GPa. These threshold pressures for melting and vaporization/degassing are modeled by ANEOS and may somewhat differ from those of real materials, although they are in fact very near to experimentally based estimates (*e.g.*, see summary in Stöffler, 1984) which are 20 GPa for quartz sand, ~30 GPa for sandstone (25% porosity) and 60 GPa for granite. Volatiles may also strongly influence melt-pressure values (it is believed that at least the upper sand layer was water saturated). Overall, however, because of the quick decay of shock pressures away from the impact point, small changes in those threshold values have small effects on total melt production.

The simulations results for a Ries-size crater are shown in Table 4. Combined with previous results (Artemieva, 2002), which exclude impacts below 30° because of the strong contamination of target melt with projectile melt, these results suggest that a 30° impact is the most favorable for tektite-type melt production. This results also suggest the need for a different approach for melt production from specific target layers compared to overall target melt (*e.g.*, Pierazzo and Melosh, 1999; Ivanov and Aremieva, 2001) characterized by maximum melt production at 30°, followed by a sharp decrease at lower impact angles.

Scaling for Layered Targets

Scaling of melt production has been the subject of many investigations (*e.g.*, O'Keefe and Ahrens, 1977; Schmidt and Housen, 1987; Bjorkman and Holsapple, 1987; Pierazzo *et al.*, 1997; Pierazzo and Melosh, 2000), resulting in scaling laws for target melt production that are widely used. Melt production reflects the trade offs between impact velocity, projectile size, and impact angle to produce a constant transient crater diameter. The decrease in projectile size eventually counteracts the increase in impact velocity by focusing the impact energy on a smaller region (decreasing the projectile's footprint), while a 30° impact angle is associated with maximum melt production. However, it is not clear how melt production scales for
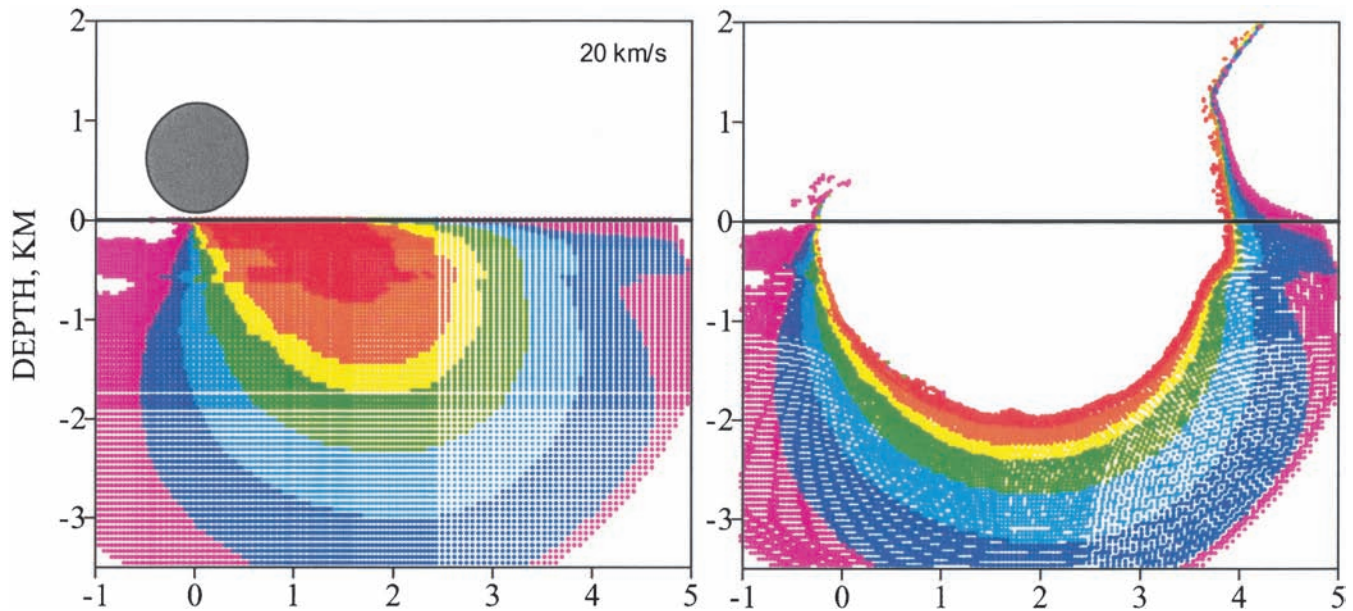
FIG. 5. Shock compression in the target for an impact at 45° with impact velocity of 20 km/s, (a) with respect to the pre-impact region (used to reconstruct the volume of material that is melted or vaporized), and (b) as the crater cavity opens up, at ~5 s after impact. Colors represent various shock states: pink = 5–20 GPa; dark blue = 20–30 GPa; light blue = 30–50 GPa; green = 50–100 GPa; yellow = 100–150 GPa; orange = 150–200 GPa; red > 250 GPa.

individual target layers, which can be important when material characteristics may affect the impact outcomes. Table 4 shows that overall impact velocity appears to play a small role in impact melting of the uppermost layer, from which tektites originate (e.g., a 45° impact produces about 0.21–0.23 km³ of melt regardless of the impact velocity used in the simulations). On the other hand, impact angle is very important: lower impact angles dramatically increase the melting of the top layers (e.g., from 0.23 km³ for a 45° impact to 0.67 km³ for a 15° impact, at 20 km/s, for the uppermost layer). This is in contrast with a maximum overall target melting (and basement melting in Table 4) at 30°. To address the effect of projectile size on melting of layers, we carried out two simulations with constant impact angle, 30°, and velocity, 20 km/s, but different projectile sizes: 1.5, and 1.9 km, corresponding to ~12.5 and ~15.5 km transient crater diameters, respectively. The results are summarized in Table 5, showing the amount of melting in each target layer estimated from the two simulations, and their ratio. For comparison, the square and cube of the ratio of the projectile diameters are 1.6 and 2.03, respectively. This test suggests that the amount of melting of finite thickness layers scales with the projectile's cross section (D^2), not its volume (D^3), as is the case for overall target melt. The only layer for which this is not the case is the basement, which indeed cannot be considered a finite-thickness layer. In this case the melt volume scales with the projectile's volume (the slightly higher ratio of melt volumes over the projectile volumes is consistent with a slightly enhanced melting due to the shock wave's interaction with the upper layer's

TABLE 5. Melt production vs. projectile size for a Ries-type layered target.

	$D_{p1} = 1.5$	$D_{p2} = 1.9$	V_{M2}/V_{M1}
Sands (40 m)	0.37	0.60	1.62
Limestone (140 m)	1.14	1.85	1.62
Sandstone (420 m)	6.27	10.00	1.59
Basement	13.44	29.20	2.17
Total	21.22	41.65	1.96

For comparison: $(D_{p2}/D_{p1})^2 = 1.6$; $(D_{p2}/D_{p1})^3 = 2.03$.

boundary). Overall, however, melt production in the basement dominates the scaling, and the total target melt production still scales with the projectile volume.

TEKTITE PRODUCTION

Finally, separate simulations have been carried out to investigate the formation and distribution of tektites formed in the Ries impact event. Previous modeling of these very special ejecta dealt mainly with the initial stage of the impact, such as shock compression of the surface material and its acceleration after decompression (Artemieva, 2001, 2002). These early studies showed that tektites (or, more accurately, high-velocity, high-temperature target melt) may be produced by high-velocity (>15 km/s) impacts into silica-rich targets with impact angles

between ~30 and 50° (Artemieva, 2001, 2002). More oblique impacts are not as efficient, because they produce target melts that are increasingly contaminated with projectile material. The main conclusion of the previous modeling work is that there is no need for special impact conditions to produce tektites (Artemieva, 2002).

We chose to focus on the simulation of a 30°, 20 km/s impact, which represents the best case scenario for tektite production, although impact angles up to ~50° may still work, but providing slightly less favorable conditions.

The previous modeling effort treated molten material as a continuum (Artemieva, 2002). This is a reasonable assumption in the early stages of crater growth and material ejection, but at some later stage the properties of individual particles (*i.e.*, mass, size, shape, individual velocity) become important. At that point the particle trajectories in the atmosphere should be defined by the hydrodynamics of two phases, including the interaction (based on momentum and heat exchange) of solid particles with the post-impact gas flow. To avoid limitations of computer capacity, we have implemented the approach of using representative tracer particles (*e.g.*, Teterev and Nemtchinov, 1993; Shuvalov, 1999, 2001): each marker describes the motion of a large number (10^5–10^{10}) of real particles, all of approximately the same parameters and trajectories. The size and shape of individual particles are influenced by many processes (*e.g.*, Melosh and Vickery, 1991; Melosh, 1984; O'Keefe and Ahrens, 1986); ideally, they should be modeled by adding a disruption module to the hydrocode. In our simplified approach, material disruption is assumed to occur when the density of the solid or molten material drops below the normal density for a given temperature within a single computational cell (*i.e.*, the material is subject to tension). The initial particle velocity is given by the hydrodynamic velocity of the cell, while the object's initial position within the cell is randomly defined. We have modeled solid particles distribution by using an empirical size distribution based on experimental studies of high-energy chemical explosions (Solov'ev; pers. comm.), with particle sizes ranging from ~1 μm to 10 cm. The diameter of molten particles were initially kept constant at 3 cm in diameter, which corresponds to the average size of tektites (O'Keefe, 1963, 1976; Montanari and Koeberl, 1999). Currently, this model has been upgraded by assuming that particle diameters are in the range of 1 cm ("hot" melt) to 3 cm ("cold" melt), while particle size drops to 0.01 cm if particles are produced by condensation from a two-phase mixture (very hot region in which vapor and melt coexist). These assumptions are based on a simple approach (Melosh and Vickery, 1991): particle size in the melt disruption process depends on the balance of local strain rates and surface tension in the melt. Higher temperature melt has a smaller surface tension thus producing smaller particles. In our simplified approach, we model 3 cm diameter particles if the temperature is around melting (1400–1500 K), and linearly decrease their size with increasing temperature, up to 1 cm diameter particles around

vaporization (~2800 K). If the particles are formed from vapor (condensation) they should be orders of magnitude smaller (Zel'dovich and Raizer, 1967). We plan to include more sophisticated models for melt disruption in the future. For simplicity, we model particles as ideal spheres (although this is not really the case for tektites). As we have two "porous quartzite" layers (sands and sandstone), we use the tracers' initial positions to determine from which precursor layer, Tertiary sands or Triassic sandstones, a particular melt is derived. These particles move together with the material, but have no influence on the flow. When the nearest tracer is from the upper layer, we define the melt (or, later, the resulting particles) as upper-layer (*i.e.*, tektite type) melt. If the nearest tracer is from the deeper sandstone layer, the melt is characterized as a siliceous melt retained inside the crater (this melt is also shown in a different color in the figures).

Figure 6 shows early stages of a Ries-type impact at 30° and 20 km/s, including particle production and their motion in the atmosphere. Only particles larger than 1 cm in diameter are shown, to avoid an overcrowding of the figure. Molten particles from the upper (40 m) quartzite layer (*i.e.*, potential tektites) are shown in red, particles from the molten projectile or deeper target melts are yellow, and solid particles are shown in black. Four seconds after the impact, practically all of the molten and vaporized upper layer (sand) material is ejected and disrupted into particles, while intensive ejection of (either molten or solid) material from deeper layers will continue for much longer.

An appreciable part of the upper layer material is vaporized and it initially starts to move as a gas or two-phase mixture; later on: however, condensation from the vapor can occur, resulting in the formation of microtektites. There is no record of microtektites associated with the Ries crater. Microtektites are typically found in deep sea sediments where they are buried and therefore preserved; however, when exposed at the surface they are subject to strong weathering processes that destroy them.

The Ries impact site is characterized by a thick sedimentary layer, from which a large amount of vapor (*e.g.*, CO_2) is shock-released. This vapor contributes to the particles acceleration, or at least, to the sustainment of their motion. The initial ejection velocities of material are rather high, up to 10 km/s, which is close to the velocity of the expanding gas. As a result, the particles are not subject to high dynamic pressures (Fig. 7) that otherwise would disrupt them into fine mist immediately after ejection. The temperature of the entraining gas is rather high, so the particles do not cool quickly during the flight (Fig. 8), allowing enough time to have them aerodynamically shaped (typical for tektites), and to lose volatiles (like water).

The initial hydrocode simulations, that include both the opening of the cavity and the atmospheric flow of material ejected from it, is carried out to ~5 s after impact (Fig. 5). In this initial stage high spatial resolution is used close to the impact point. However, to resolve the atmospheric flow of the
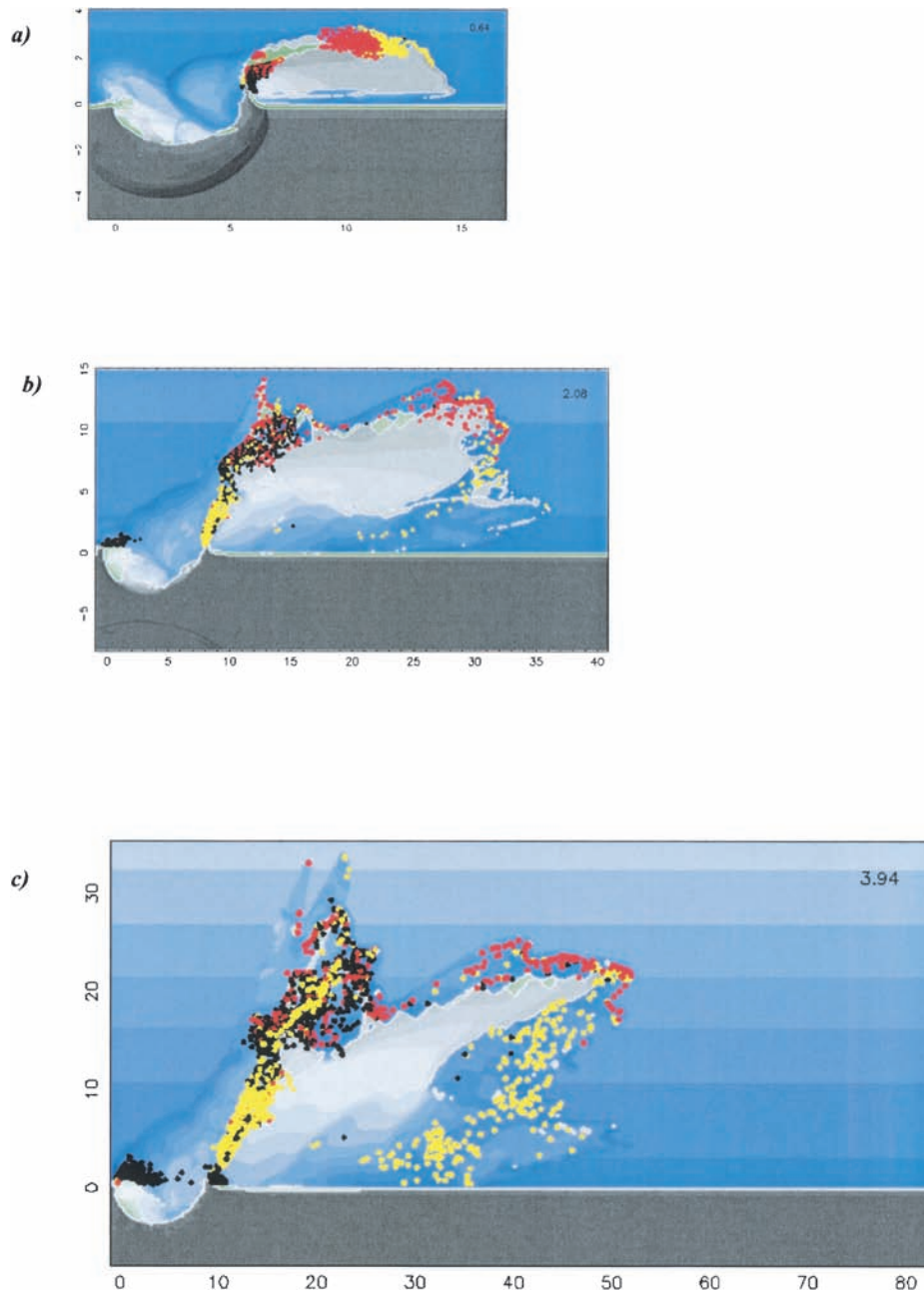
FIG. 6. Tektite ejection model results for a 30° impact and impact speed of 20 km/s at (a) 0.6 s, (b) 2 s, and (3) 3.9 s after the impact. Red = molten upper layer material (possible tektites). Yellow = molten target materials (no tektites). Black = solid target material.

expanding vapor plume and the imbedded particles we must model a rather large region—hundreds of kilometers in both height and downrange direction, which can only be done at a much lower spatial resolution. This is acceptable for modeling high-velocity ejecta, but it affects our ability to model accurately low-velocity ejecta.

Between 20 and 40 s after contact, the majority of the particles has reached altitudes above ~50 km. We exclude from the model particles exceeding altitudes of ~200 km,

corresponding to material that will reach worldwide distribution (some of these particles even reach escape velocities). At this point, full-scale hydrocode modeling becomes computationally too expensive and very inefficient, because typical time steps in the hydrocode simulation are <0.1 s. We therefore turn off the hydrodynamic flow at this stage and consider the motion of particles in an undisturbed atmosphere (i.e., using pre-impact stratification and zero gas velocity). In reality, impact-related perturbations are still present in the atmosphere, but they can
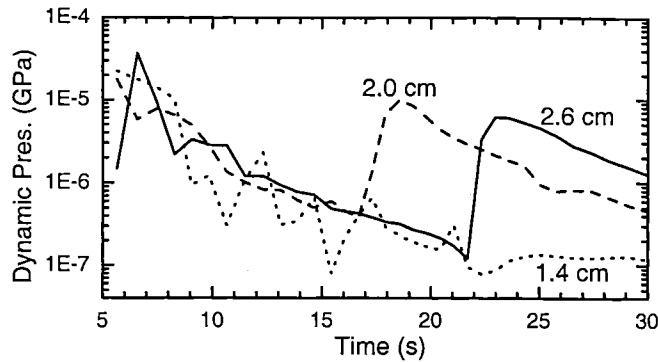
FIG. 7. Dynamic pressure *vs.* time for a tektite-type particles of different sizes. The solid line represents a tektite 1.3 cm in diameter, dashed line a tektite 1.0 cm in diameter, and dotted line a tektite 0.7 cm in diameter.
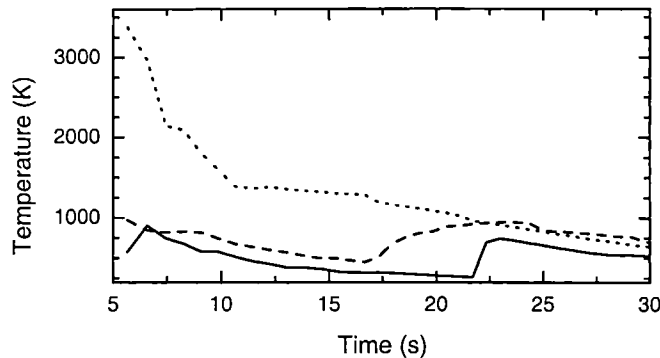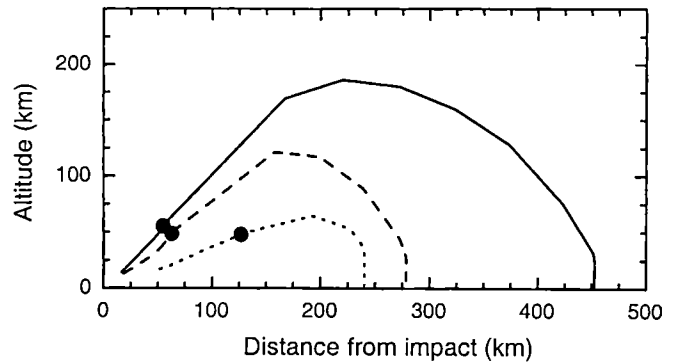

FIG. 9. Trajectories of the tektite-type particles shown in Figs. 7 and 8. Circles mark the end of the hydrodynamic simulations (~30 s after the impact). From that point on the trajectories represent the motion of particles in an undisturbed atmosphere.

FIG. 8. Temperature *vs.* time for the same tektite-type particles of Fig. 7.

reality, the Tertiary sand cover at the Ries was probably patchy and of variable thickness; thus the estimated 10 Mt of tektites is an upper limit. It is remarkable, however, that such an estimate is only about a factor of 2 larger than recent geological estimates of ~5 Mt (Montanari and Koeberl, 1999). The tektite-type material is distributed up to 400–500 km away from the impact, in a fan of ~75° symmetrically distributed with respect to the downrange direction. The calculated final distribution of tektites is in principle but not in detail similar to the distribution of the real moldavites. This indicates that the production and distribution of tektites can be explained by impact cratering mechanics and the physics of motion of particles in a gas flow, without the necessity of invoking special impact conditions, such as very low impact angles or high impact velocity.

SUMMARY AND CONCLUSIONS

On the basis of a detailed assessment of the geological, petrographic, geographical and chronological characteristics of three related impact phenomena—Ries crater, Steinheim crater, and the moldavite tektite strewn field—a numerical modeling study has been performed to evaluate wether a single collsional event could have been responsible for the formation of the two craters and the tektites. The results of this study illustrate for the first time a comprehensive and well-founded basis for such a scenario: a binary asteroid consisting of two bodies, about 1.5 and 0.15 km in diameter, with a pre-impact separation of some tens of kilometers impacted the target area at an angle around 30–50° from the surface in a west-southwest–east-northeast direction. The two objects formed the Steinheim basin and the Ries crater sequentially and ejected two types of melt from the Ries target downrange towards east-northeast: tektite melt originating from a sand-rich surface layer to distances up to 450 km, and melt from the main melt zone in the crystalline basement of the Ries deposited as decimeter-sized lumps on the inner slope of the east-northeast rim of the Ries crater. The total mass of tektite melt calculated is near 10 Mt
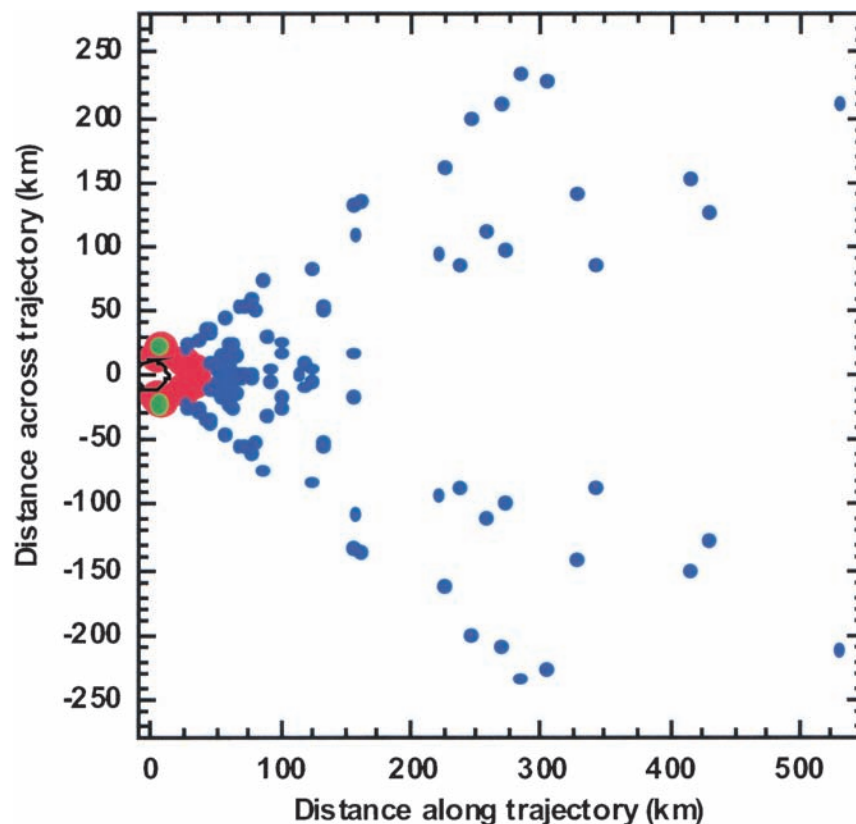
be neglected without affecting the final result; (to test this we continued a full-scale calculation up to 6 min after the impact, without finding visible changes in the final tektites deposition). The particles end up moving through the undisturbed atmosphere with low velocity (tens of meters per second, typical settling velocity for particles of that size and shape). It usually takes 5–30 min for particles to land on the surface. Figure 9 shows the complete trajectories of the same tektite-type particles shown in Figs. 7 and 8. The final surface distribution of the modeled tektites is shown in Fig. 10, where different color dots represent different tektite masses. The symmetry with respect to the downrange direction is a direct consequence of the bilateral symmetry adopted for the simulation. About 16 Mt of tektite-type material (*i.e.*, excluding material that exceeded heights of 200 km, as discussed above) is produced in the simulation. A fraction of this material (~6 Mt) lands close to the impact point, indicating it is part of the ejecta curtain that surrounds the crater (usually extending about two radii away from the crater), and is therefore mixed with the other target melts. The remaining ~10 Mt could be identified as tektites. It should be kept in mind that the uppermost (tektite-forming) layer was modeled as a 40 m thick continuum (Table 2). In

FIG. 10. Final distribution of tetkite-type particles on the surface for a 30°, 20 km/s impact. The origin is located at the impact point. Colors represent mass of material deposited at a given location: blue = 0.01–0.1 Mt; green = 0.1–1.0 Mt; red = 1.0–10.0 Mt. The circle roughly corresponds to the rim of the Ries crater.

(maximum estimate based on 40 m of continuous Tertiary sands) which compares well with the 5 Mt estimated from field observations (Montanari and Koeberl, 1999). It is obvious from the results that the three-dimensional numerical simulation of the impact and ejection processes can explain the observations with a relatively good precision. The detailed arguments for the model-based interpretation of the field observations are as follows.

Integration of the equation of motion of different size impactors (similarly to Melosh and Stansberry, 1991) commensurate with the Ries and Steinheim craters consistently produce maximum separation distances of the two bodies at the Earth's surface which are more than 2 orders of magnitude smaller than the distance between the Ries and Steinheim, ~42 km. Atmospheric breakup for the creation of two simultaneously impacting objects is thus ruled out. This then favors the theory of a binary asteroid with a pre-impact separation similar to the distance between the two craters, and ~1 order of magnitude difference in mass between the two components (e.g., Melosh and Stansberry, 1991). The Ida–Dactyl system (Davis et al., 1996) is the most famous case of a well-separated binary asteroid in which one object is orders of magnitude larger than the other. It must be pointed out, however,

that the Ida–Dactyl system is much larger than the potential Ries–Steinheim binary system. Recently, a binary system has been observed where the primaries are some 0.2–0.8 km in size, not unlike the Ries case (Margot et al., 2002).

The results of a series of three-dimensional hydrocode simulations that varied impact angle and impact velocity to produce a Ries-type impact of constant transient crater diameter supported by previous results indicate 30° as the most favorable angle for near-surface melting and the ejection of tektites representing melt with low projectile contamination from the uppermost target layer. For constant resulting transient craters, impact velocity has a smaller influence on the amount of melt and vaporization than has the impact angle (Table 4).

The modeling of the motion of impact-produced tektite-type particles through the atmosphere allows to address mainly the "mechanical" component of the complex tektite problem, that is the possibility of ballistically transporting particles hundreds of kilometers away from the parent crater. At this point, we cannot address the "geochemical" component of the problem in detail although the calculated pressure-temperature conditions (Figs. 7 and 8) are consistent with some characteristics, such as low water content, homogeneity and scarcity of vesicles of tektites. A simulation of a Ries-sized

impactor at 30° and 20 km/s produces a relatively narrow-angle distribution of tektite-type material downrange, in agreement with that observed for the moldavites strewn field. The exact width of the fan, ~75° for the modeled 30° impact, is a funtion of impact angle; to characterize such a dependence requires to extend the (time and computationally) extensive simulation carried out for a 30° impact to other impact angles in the range 30–50°. However, we expect that wide variations of the angle of this fan will not occur for the expected impact angle of 30–50°. Although the modeled particle distribution extends over a continuous radial range, somewhat different from the known distribution of the moldavites, these results represent an important step toward a better understanding of the moldavite strewn field. The lack of tektites at ranges up to 200 km can be easily explained by the lack of 15 Ma old host sediments that would be contemporaneous with the Ries event in the entire region between the Ries and the western border region of the Czech Republic (Fig. 1). Several other factors could have influenced the final distribution of the moldavites. Besides projectile-related factors, such as projectile size, impact angle and impact velocity, target characteristics are going to affect the final distribution of the moldavites, such as local variations in the stratigraphy and a discontinuous distribution of the upper layer of Tertiary sands in the Ries, and the size distribution of the melt particles. The 57° fan where the moldavites are found today may have been slightly modified from the original distribution because of mechanisms like erosion and surface transport of tektites since their formation. Therefore, we consider the estimated 75° fan to be in good agreement with the observed distribution.

Another outcome of the modeling of the Ries impact crater formation and of the motion of melt inside and outside the crater (Figs. 4, 5 and 6) is the preferred flow of melt from the main melt zone of the crystalline basement downrange towards the east-northeast rim. This explains well the occurrence of coherent impact melt patches in a restricted zone of the downrange rim of the Ries crater (Fig. 2). These melt bodies do not occur anywhere else in the Ries, and their somewhat enigmatic nature has been solved by the present simulations.

Editorial handling: E. Asphaug

REFERENCES

AHRENS T. J. AND O'KEEFE J. D. (1977) Equations of state and impact-induced shock wave attenuation on the moon. In *Impact and Explosion Cratering* (eds. D. J. Roddy, R. O. Pepin and R. B. Merrill), pp. 639–656. Pergamon Press, New York, New York, USA.

ARTEMIEVA N. A. (2001) Tektite production in oblique impacts (abstract). *Lunar Planet. Sci.* **32**, #1216, Lunar and Planetary Institute, Houston, Texas, USA (CD-ROM).

ARTEMIEVA N. A. (2002) Tektite origin in oblique impact: Numerical modeling. In *Meteorite Impacts in Precambrian Shields* (eds. Y. Plado and L. Pesonen), pp. 257–276. Springer Verlag, Berlin, Germany.

ARTEMIEVA N. A. AND SHUVALOV V. V. (1994) Oblique impact: Atmospheric effects (abstract). *Lunar Planet. Sci.* **25**, 39–40.

ARTEMIEVA N. A. AND SHUVALOV V. V. (2001) Motion of fragmented meteoroid through the planetary atmosphere. *J. Geophys. Res.* **106**, 3297–3310.

BJORKMANN M. D. AND HOLSAPPLE K. A. (1987) Velocity scaling impact melt volume. *Intl. J. Impact Eng.* **5**, 155–163.

BOLTEN R. AND MÜLLER D. (1969) Das Tertiär im Nördlinger Ries und in seiner Umgebung. *Geologica Bavarica* **61**, 87–130.

DAVID E. (1966) Flight of tektites from meteorite impact. *Zeitschr. Naturforschg.* **21a**, 1131–1137.

DAVIS D. R., CHAPMAN C. R., DURDA D. D., FARINELLA P. AND MARZARI F. (1996) The formation and collisional/dynamical evolution of the Ida/Dactyl system as part of the Koronis family. *Icarus* **120**, 220–230.

ENGELHARDT W. VON (1967) Chemical composition of Ries glass bombs. *Geochim. Cosmochim. Acta* **31**, 1677–1689.

ENGELHARDT W. VON (1972) Shock produced rock glasses from the Ries Crater. *Contrib. Mineral. Petrol.* **36**, 265–292.

ENGELHARDT W. VON (1997) Suevite breccia of the Ries impact crater, Germany: Petrography, chemistry, and shock metamorphism of crystalline clasts. *Meteorit. Planet. Sci.* **32**, 545–594.

ENGELHARDT W. VON, STÖFFLER D. AND SCHNEIDER W. (1969) Petrologische Untersuchungen im Ries. *Geologica Bavarica* **61**, 229–295.

ENGELHARDT W. VON, LUFT E., ARNDT J., SCHOCK H. AND WEISKIRCHNER W. (1987) Origin of moldavites. *Geochim. Cosmochim. Acta* **51**, 1425–1443.

GALL H. AND MÜLLER D. (1975) Reutersche Blöcke—Ausseralpine Fremdgesteine unterschiedlicher Herkunft in jungtertiären und quartären Sedimenten Südbayerns. *Mitt. Bayer. Staatssamml. Paläontol. Hist. Geol.* **15**, 207–228.

GENTNER W. AND WAGNER G. A. (1969) Altersbestimmungen an Riesgläsern und Moldaviten. *Geologica Bavarica* **61**, 296–303.

GENTNER W., LIPPOLT H. J. AND SCHAEFFER O. A. (1963) Argonbestimmungen an Kaliummineralien—XI. Die Kalium-Argon-Alter der Gläser des Nördlinger Rieses und der böhmisch-mährischen Tektite. *Geochim. Cosmochim. Acta* **27**, 191–200.

GRAUP G. (1978) *Das Kristallin des Nördlinger Ries. Petrographische Zusammensetzunng und Auswurfsmechanismus der kristallinen Trümmermassen, Struktur des kristallinen Untergrundes und Beziehungen zum Moldanubikum.* Ferdinand Enke Verlag, Stuttgart, Germany. 190 pp.

GRAUP G. (1999) Carbonate silicate immiscibility upon impact melting: Ries crater, Germany. *Meteorit. Planet. Sci.* **34**, 425–438.

GROSCHOPF P. AND REIFF W. (1971) Vorläufige Ergebnisse der Forschungsbohrung 1970 im Steinheimer Becken (Schwäbische Alb). *Jahresheft. Geolog. Landesamt Baden-Württemberg, Freiburg* **13**, 223–226.

HORN P., MUELLER-SOHNIUS D., KOEHLER H. AND GRAUP G. (1985) Rb-Sr systematics of rocks related to the Ries, Germany. *Earth Planet. Sci. Lett.* **75**, 384–392.

HÖRZ F., OSTERTAG R. AND RAINEY D. A. (1983) Bunte Breccia of the Ries: Continuous deposit of large impact craters. *Rev. Geophys. Space Phys.* **21**, 1667–1725.

HÜTTNER R. AND SCHMIDT-KALER H. (1999) Erläuterungen zur geologischen Karte des Rieses 1:50000. *Geologica Bavarica* **104**, 7–76.

IVANOV B. A. AND ARTEMIEVA N. A. (2001) Transient cavity scaling for oblique impacts (abstract). *Lunar Planet. Sci.* **32**, #1327, Lunar and Planetary Institute, Houston, Texas, USA (CD-ROM).

KIEFFER S. W. AND SIMONDS C. H. (1980) The role of volatiles and lithology in the impact cratering process. *Rev. Geophys. Space Physics* **18**, 143–181.

KOEBERL C., BRANDSTÄTTER F., NIEDERMAYER G. AND KURAT G. (1988) Moldavites from Austria. *Meteoritics* **23**, 325–332.

LANGE J-M. (1990) Tektite der Niederlausitz. *Natur und Landschaft Bezirk Cottbus NLBC* **12**, 77–94.

LANGE J-M. (1996) Tektite glasses from Lusatia (Lausitz), Germany. *Chem. Erde* **56**, 498–510.

MARGOT J. I., NOLAN M. C., BENNER L. A. M., OSTRO S. J., JURGENS R. F., GIORGINI J. D., SLADE M. A., HOWELL E. S. AND CAMPBELL D. B. (2002) Radar discovery and characterization of binary near-Earth asteroids (abstract). *Lunar Planet. Sci.* **33**, #1849, Lunar and Planetary Institute, Houston, Texas, USA (CD-ROM).

MCGLAUN J. M., THOMPSON S. L. AND ELRICK M. G. (1990) CTH: A three-dimensional shock wave physics code. *Intl. J. Impact Eng.* **10**, 351–360.

MELOSH H. J. (1984) Impact ejection, spallation, and the origin of meteorites. *Icarus* **59**, 234–260.

MELOSH H. J. (1989) *Impact Cratering: A Geological Process.* Oxford Univ. Press, New York, New York, USA. 246 pp.

MELOSH H. J. AND STANSBERRY J. (1991) Doublet craters and the tidal disruption of binary asteroids. *Icarus* **94**, 171–179.

MELOSH H. J. AND VICKERY A. M. (1991) Melt droplet formation in energetic impact events. *Nature* **350**, 494–497.

MONTANARI A. AND KOEBERL C. (1999) *Impact Stratigraphy: The Italian Record.* Springer-Verlag, Berlin, Germany. 364 pp.

MORGAN J. W., JANSSENS M-J., HERTOGEN J., GROS J. AND TAKAHASHI H. (1979) Ries impact crater, southern Germany: Search for meteoritical material. *Geochim. Cosmochim. Acta* **43**, 803–815.

O'KEEFE J. A., ED. (1963) *Tektites.* Univ. Chicago Press, Chicago, Illinois, USA. 228 pp.

O'KEEFE J. A. (1976) *Tektites and their Origin.* Elsevier, New York, New York, USA. 254 pp.

O'KEEFE J. D. AND AHRENS T. J. (1977) Impact-induced energy partitioning, melting, and vaporization on terrestrial planets. *J. Geophys. Res.* **92**, 1849–1870.

O'KEEFE J. D. AND AHRENS T. J. (1986) The size distributions of fragments ejected at a given velocity from impact craters (abstract). *Lunar Planet. Sci.* **17**, 1004–1005.

PASSEY Q. R. AND MELOSH H. J. (1980) Effects of atmospheric breakup on crater field formation. *Icarus* **42**, 211–233.

PIERAZZO E. AND MELOSH H. J. (1999) Hydrocode modeling of Chicxulub as an oblique impact event. *Earth Planet. Sci. Lett.* **165**, 163–176.

PIERAZZO E. AND MELOSH H. J. (2000) Melt production in oblique impacts. *Icarus* **145**, 252–261.

PIERAZZO E., VICKERY A. N. AND MELOSH H. J. (1997) A reevaluation of impact melt production. *Icarus* **127**, 408–423.

PIERAZZO E., KRING D. A. AND MELOSH H. J. (1998) Hydrocode modeling of the Chicxulub impact event and the production of climatically active gases. *J. Geophys. Res.* **103**, 28 607–28 625.

PIERAZZO E., ARTEMIEVA N. A. AND SPITALE J. N. (2001) The Ries impact event: A tale of two hydrocodes (abstract). In *Impact Markers in the Stratigraphic Record. Abstracts of the 6th ESF Impact Workshop* (eds. F. Martinez-Ruis, M. Ortera-Huertas and I. Palomo), pp. 87–88. ESF, Granada, Spain.

POHL J., STÖFFLER D., GALL H. AND ERNSTSON K. (1977) The Ries impact crater. In *Impact and Explosion Cratering* (eds. D. J. Roddy, R. O. Pepin and R. B. Merrill), pp. 343–404. Pergamon Press, New York, New York, USA.

REIFF W., ED. (1979) *Guidebook to the Steinheim Basin Impact Crater.* Geol. Landesamt Baden-Württemberg, Stuttgart, Germany. 32 pp.

SCHMIDT R. M. AND HOUSEN K. R. (1987) Some recent advances in the scaling of impact and explosion cratering. *Intl. J. Impact Eng.* **5**, 543–560.

SCHNELL T. (1926) Der bayrische Trass und seine Entstehung. In *Das Problem des Rieses, zugleich Führer zu geologischen Ausflügen in der Umgebung von Nördlingen, herausgegeben vom Oberrheinischen Geologischen Verein anläßlich seiner Tagung im Frühjahr 1924 (Nördlingen).* Jahresber. Oberrhein. Geol. Ver. N. F. **14**, 222–279.

SHUVALOV V. (1999) Multi-dimensional hydrodynamic code SOVA for interfacial flows: Application to the thermal layer effect. *Shock Waves* **9**, 381–390.

SHUVALOV V. (2001) Dust ejection induced by small meteoroids impacting martian surface (abstract). *Lunar Planet. Sci.* **32**, #1126, Lunar and Planetary Institute, Houston, Texas, USA (CD-ROM).

STÄHLE V. (1972) Impact glasses from the suevite of the Nördlinger Ries. *Earth Planet. Sci. Lett.* **17**, 275–293.

STAUDACHER T., JESSBERGER E. K., DOMINIK T. K. AND SCHAEFFER O. A. (1982) ^{40}Ar-^{39}Ar ages of rocks and glasses from the Nördlinger Ries crater and the temperature history of impact breccias. *J. Geophys.* **51**, 1–11.

STÖFFLER D. (1984) Glasses formed by hypervelocity impact. *J. Non-Cryst. Solids* **67**, 465–502.

STÖFFLER D. AND OSTERTAG R. (1983) The Ries impact crater. *Fortschr. Mineral.* **61**, 71–116.

STÖFFLER D., ARTEMIEVA N. A., PIERAZZO E. AND IVANOV B. A. (2001) Ries crater, Germany: Geology and numerical modeling of impact cratering (abstract). *Meteorit. Planet. Sci.* **36 (Suppl.)**, A199.

STÖFFLER D., ARTEMIEVA N. A. AND PIERAZZO E. (2002) Modeling the Ries-Steinheim impact event and the formation of the moldavite strewn-field (abstract). *Lunar Planet. Sci.* **33**, #1871, Lunar and Planetary Institute, Houston, Texas, USA (CD-ROM).

TETEREV A. V. AND NEMTCHINOV I. V. (1993) The sand bag model of the dispersion of the cosmic body in the atmosphere (abstract). *Lunar Planet. Sci.* **24**, 1415–1416.

THOMPSON S. L. AND LAUSON H. S. (1972) *Improvements in the Chart D Radiation-Hydrodynamic Code III: Revised Analytical Equation of State. SC-RR-61 0714*, Sandia Nat. Labs., Albuquerque, New Mexico, USA. 119 pp

VAND V. (1963) Ries Kessel and Steinheim Basin. *Mineral Industries Expt. Sta., Pennsylvania* **32**, 1–8.

VENNEMANN T. W., MORLOK A., ENGELHARDT W. VON AND KYSER K. (2001) Stable isotope composition of impact glasses from the Nördlinger Ries impact crater, Germany. *Geochim. Cosmochim. Acta* **65**, 1325–1336.

ZEL'DOVICH Y. B. AND RAIZER Y. P (1967) *The Physics of Shock Waves and High Temperature Hydrodynamic Phenomena.* Adademic Press, New York, New York, USA. 916 pp.